

SEEDS DIRECT IMAGING OF THE RV-DETECTED COMPANION TO V450 ANDROMEDAE,
AND CHARACTERIZATION OF THE SYSTEM.

K. G. HELMINIAK^{1,2}, M. KUZUHARA^{3,4,5}, K. MEDE⁶, T. D. BRANDT^{7,8}, R. KANDORI⁴, T. SUENAGA^{4,9}, N. KUSAKABE⁵, N. NARITA^{5,4,9,6}, J. C. CARSON¹⁰, T. CURRIE¹, T. KUDO¹, J. HASHIMOTO⁵, L. ABE¹¹, E. AKIYAMA⁴, W. BRANDNER¹², M. FELDT¹², M. GOTO¹³, C. A. GRADY^{14,15,16}, O. GUYON^{1,17}, Y. HAYANO¹, M. HAYASHI⁴, S. S. HAYASHI^{1,9}, T. HENNING¹², K. W. HODAPP¹⁸, M. ISHII⁴, M. IYE⁴, M. JANSON¹⁹, G. R. KNAPP²⁰, J. KWON⁶, T. MATSUO²¹, M. W. McELWAIN¹⁴, S. MIYAMA²², J.-I. MORINO⁴, A. MORO-MARTIN^{12,23}, T. NISHIMURA¹, T. RYU^{9,4}, T.-S. PYO¹, E. SERABYN²⁴, H. SUTO^{4,5}, R. SUZUKI⁴, Y. H. TAKAHASHI^{6,4}, M. TAKAMI²⁵, N. TAKATO¹, H. TERADA⁴, C. THALMANN²⁶, E. L. TURNER^{20,27}, M. WATANABE²⁸, J. WISNIEWSKI²⁹, T. YAMADA³⁰, H. TAKAMI⁴, T. USUDA⁴, AND M. TAMURA^{6,4,5}

Draft version September 5, 2018

ABSTRACT

We report the direct imaging detection of a low-mass companion to a young, moderately active star V450 And, that was previously identified with the radial velocity method. The companion was found in high-contrast images obtained with the Subaru Telescope equipped with the HiCIAO camera and AO188 adaptive optics system. From the public ELODIE and SOPHIE archives we extracted available high-resolution spectra and radial velocity (RV) measurements, along with RVs from the Lick planet search program. We combined our multi-epoch astrometry with these archival, partially unpublished RVs, and found that the companion is a low-mass star, not a brown dwarf, as previously suggested. We found the best-fitting dynamical masses to be $m_1 = 1.141^{+0.037}_{-0.091}$ and $m_2 = 0.279^{+0.023}_{-0.020}$ M_{\odot} . We also performed spectral analysis of the SOPHIE spectra with the iSpec code. The *Hipparcos* time-series photometry shows a periodicity of $P = 5.743$ d, which is also seen in SOPHIE spectra as an RV modulation of the star A. We interpret it as being caused by spots on the stellar surface, and the star to be rotating with the given period. From the rotation and level of activity, we found that the system is 380^{+220}_{-100} Myr old, consistent with an isochrone analysis (220^{+2120}_{-90} Myr). This work may serve as a test case for future studies of low-mass stars, brown dwarfs and exoplanets by combination of RV and direct imaging data.

Subject headings: binaries: spectroscopic — binaries: visual — stars: imaging — stars: low-mass — stars: individual (V450 And)

xysiek@naoj.org

¹ Subaru Telescope, National Astronomical Observatory of Japan, 650 N. A'ohoku Place, Hilo, HI 96720, USA

² Subaru Fellow

³ Department of Earth and Planetary Sciences, Tokyo Institute of Technology, Ookayama, Meguro-ku, Tokyo, 152-8551, Japan

⁴ National Astronomical Observatory of Japan, 2-21-1, Osawa, Mitaka, Tokyo, 181-8588, Japan

⁵ Astrobiology Center of NINS, 2-21-1 Osawa, Mitaka, Tokyo, 181-8588, Japan

⁶ Department of Astronomy, University of Tokyo, 7-3-1, Hongo, Bunkyo-ku, Tokyo, 113-0033, Japan

⁷ Astrophysics Department, Institute for Advanced Study, Princeton, NJ, USA

⁸ NASA Sagan Fellow

⁹ Department of Astronomical Science, SOKENDAI (The Graduate University for Advanced Studies), 2-21-1 Osawa, Mitaka, Tokyo, 181-8588, Japan

¹⁰ Department of Physics and Astronomy, College of Charleston, 66 George St., Charleston, SC 29424, USA

¹¹ Laboratoire Lagrange (UMR 7293), Université de Nice-Sophia Antipolis, CNRS, Observatoire de la Côte d'Azur, 28 Avenue Valrose, F-06108 Nice Cedex 2, France

¹² Max Planck Institute for Astronomy, Königstuhl 17, 69117 Heidelberg, Germany

¹³ Universitäts-Sternwarte München, Ludwig-Maximilians-Universität, Scheinerstr. 1, 81679 München, Germany

¹⁴ Exoplanets and Stellar Astrophysics Laboratory, Code 667, Goddard Space Flight Center, Greenbelt, MD 20771, USA

¹⁵ Eureka Scientific, 2452 Delmer, Suite 100, Oakland, CA 94602, USA

¹⁶ Goddard Center for Astrobiology

¹⁷ Steward Observatory, University of Arizona, 933 N Cherry Ave., Tucson, AZ 85721, USA

¹⁸ Institute for Astronomy, University of Hawaii, 640 N. A'ohoku Place, Hilo, HI 96720, USA

¹⁹ Department of Astronomy, Stockholm University, AlbaNova University Center, SE-10691, Stockholm, Sweden

²⁰ Department of Astrophysical Science, Princeton University, Peyton Hall, Ivy Lane, Princeton, NJ 08544, USA

²¹ Department of Earth and Space Science, Graduate School of Science, Osaka University, 1-1 Machikaneyamacho, Toyonaka, Osaka, 560-0043, Japan

²² Hiroshima University, 1-3-2, Kagamiyama, Higashihiroshima, Hiroshima, 739-8511, Japan

²³ Department of Astrophysics, CAB-CSIC/INTA, 28850 Torrejón de Ardoz, Madrid, Spain

²⁴ Jet Propulsion Laboratory, California Institute of Technology, Pasadena, CA, 171-113, USA

²⁵ Institute of Astronomy and Astrophysics, Academia Sinica, P.O. Box 23-141, Taipei 10617, Taiwan

²⁶ Swiss Federal Institute of Technology (ETH Zurich), Institute for Astronomy, Wolfgang-Pauli-Strasse 27, CH-8093 Zurich, Switzerland

²⁷ Kavli Institute for Physics and Mathematics of the Universe, The University of Tokyo, 5-1-5, Kashiwanoha, Kashiwa, Chiba, 277-8568, Japan

²⁸ Department of Cosmosciences, Hokkaido University, Kita-ku, Sapporo, Hokkaido, 060-0810, Japan

²⁹ H. L. Dodge Department of Physics & Astronomy, University of Oklahoma, 440 W Brooks St Norman, OK 73019, USA

³⁰ Astronomical Institute, Tohoku University, Aoba-ku, Sendai, Miyagi, 980-8578, Japan

1. INTRODUCTION

For nearly two decades the radial velocity (RV) technique was the most effective one in discovering extrasolar planets and brown dwarfs, as it was among the first techniques capable of detecting sub-stellar-mass objects orbiting normal stars. Regular surveys began in the 1980-s (Fischer et al. 2014) and brought first results relatively early (Latham et al. 1989; Mayor & Queloz 1995), although these were initially limited to relatively short period orbits, owing primarily to the time span of the observations. Outside of indirect detections, the direct imaging technique has been successful in exoplanet detection for over a decade now (Chauvin et al. 2004), but is still limited to objects relatively distant from the parent star, even despite a tremendous improvement in recent years that allowed us to discover less massive planets on closer orbits (Marois et al. 2008; Lagrange et al. 2009; Rameau et al. 2013; Currie et al. 2014). Only very recently, thanks to the long-time coverage of RV data, and development of new generation instruments for both RV measurements and high contrast imaging at narrow separations, have the discovery spaces started to overlap, allowing for some objects to be detectable by both techniques. This opens new possibilities in characterization of extrasolar planets, brown dwarfs and low-mass stars. Only a few examples of RV and imaging detections of a companion have been known to date, (i.e. Crepp et al. 2012a,b, 2013b,a, 2014; Ryu et al. 2016, also: J. Hagelberg et al. 2016, in preparation) but their characterisations are either inadequate or uncertain due to incomplete data coverage of the orbit, or because the uncertainties in distance and mass of the primary were not adequately included in the final error budget. A notable case is, however, HD 16760b, first reported with RV measurements by Sato et al. (2009) and Bouchy et al. (2009), and later detected in Keck sparse aperture masking observations by Evans et al. (2012). Initial discoveries indicated a minimum mass at the border between the planetary and brown dwarf regime: 13.13(56) and 14.3(9) M_J for Sato et al. and Bouchy et al., respectively. The Keck data revealed a low-inclination orbit, and a companion mass of 0.28(4) M_\odot , but this result was not obtained from a simultaneous fit to RV and astrometric data, and the mass of the primary was assumed. It shows, however, how inaccurate the RV-based lower limits can be, and how important it is to supplement RV detections with astrometric data (see also Wilson et al. 2016).

In this paper we present an example where RV measurements span almost a whole orbital period, which allows us to obtain secure dynamical masses of both stars, and perform meaningful comparisons with the latest stellar evolution models. For the first time, the orbital fit is obtained from all data simultaneously, and masses of both components are directly calculated. Basic information about the target are given in Section 2. Section 3 describes the observational data used in this work. Orbital and spectral analysis are described in Sections 4 and 5, respectively. In Section 6 we discuss the activity and age of the system, and summarise our work in Section 7.

2. THE TARGET

V450 And (HD 13507, HIP 10321, BD+39 496; $\alpha = 02^h 12^m 55^s.0053$, $\delta = +40^\circ 40' 06''.0247$; van Leeuwen

2007) is a known BY Dra type variable. It is a G-type dwarf (Gray et al. 2003), located about 27 pc from the Sun ($\varpi = 37.25 \pm 0.55$ mas; van Leeuwen 2007), with a V-band apparent magnitude of 7.21 mag (Høg et al. 2000). It also forms a common-proper-motion pair with another BY Dra type star V451 And (HD 13531, HIP 10339), and possibly belongs to the Castor moving group (Montes et al. 2001; Caballero 2010).

The low-mass companion on a long-period orbit was first announced by Perrier et al. (2003, hereafter P03) in the Appendix of their paper. A preliminary fit was performed on 19 ELODIE measurements spanning from January 1998 to December 2002. P03 obtained an orbital period of $\simeq 3000$ days, a small eccentricity of 0.14, a companion minimum mass of 52 M_J , and a projected major semi-axis of 4.3 AU, or 164 mas at the distance to the system, assuming the mass of the host to be 1.09 M_\odot . They had, however, poor coverage of the true orbital period, resulting in an underestimation of companion mass. They also searched for the secondary with adaptive optics imaging, but failed to identify it in their data, possibly because it was close to pericenter at that time. More such attempts were made later, but again without success, either because of the unfortunate location of the secondary close to the primary (Metchev & Hillenbrand 2009), or lack of sufficient sensitivity (Tokovinin 2014; Riddle et al. 2015). We present the first positive detection of V450 And B with high-contrast imaging.

3. OBSERVATIONS AND DATA

3.1. SEEDS Observations

We observed V450 And as part of the Strategic Exploration of Exoplanets and Disks with Subaru (SEEDS; Tamura 2009) survey, which has searched for exoplanets and imaged circumstellar disks around hundreds of nearby stars (e.g., Thalmann et al. 2011; Hashimoto et al. 2012; Janson et al. 2013). One category of SEEDS targets consists of young nearby stars that can be age-dated using their rotation periods or chromospheric activities as clocks (see Kuzuhara et al. 2013), and V450 And is included in this category (we discuss the star's age in Sections 6.2 and 6.3). Its science case, however, also resembles the category of targets which are known to have inner planets or a long-term RV trend (Narita et al. 2010, 2012; Ryu et al. 2016).

We observed V450 And with the HiCIAO camera (Suzuki et al. 2010), a high-contrast imaging instrument on the Subaru Telescope. The adaptive optics system AO188 (Hayano et al. 2010) was used to reduce the image degradation caused by atmospheric turbulence and improve the Strehl ratio. AO188's atmospheric dispersion corrector (ADC; Egner et al. 2010) removed the chromaticity of atmospheric refraction. None of our observations used a focal plane mask, but all were performed with a Lyot stop in the pupil plane. HiCIAO's original Lyot stop was replaced in September 2013 with a larger, circular pupil stop (in other words, smaller pupil-plane mask) to increase throughput and improve angular resolution.

We observed the star at four epochs, controlling the image rotator to fix the pupil rotation relative to the camera (angular differential imaging, or ADI, mode, Marois et al. 2006). Each observing sequence consisted

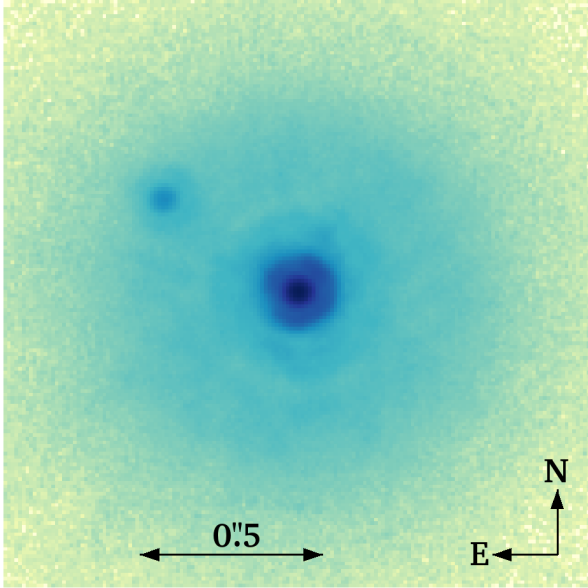


FIG. 1.— H -band image of V450And showing its M dwarf companion about $0''.44$ to the northeast. The stretch is logarithmic; the companion is about 40 times fainter in the H -band than the G5 primary. The figure is a composite image of 50 single, unsaturated frames, all taken on 8 January 2015. The total exposure time is 575 sec.

of longer sequences of frames in which the central star’s point-spread function (PSF) was saturated, and shorter sequences using neutral density filters to avoid saturation. The unsaturated images were taken sparsely during one visit. The saturated images were used to search for faint companions (Kuzuhara et al. 2016, in preparation) while the unsaturated images were used for image registration and flux calibration. We discovered one companion candidate, about 40 times fainter than V450 And in the H -band; follow-up observations confirmed it as a low-mass stellar companion. Figure 1 shows the pair V450 And AB. Because of the modest contrast between the primary and secondary, we used only unsaturated images in each observing sequence to measure the astrometry of the system and to track its orbital motion. Table 1 summarizes the unsaturated data used in our analysis of the V450 And system; our analysis makes no use of saturated imaging. The next section discusses the measurement and calibration of the astrometry in each observing sequence.

3.2. Data Reductions and Astrometry

At an H -band contrast of only ~ 40 , V450 And B is bright enough to be detected in the unsaturated short-exposure data sets. This enables us to simultaneously obtain very accurate positions and photometry of both stars: our simultaneous relative photometry is unaffected by temporal variations in the Strehl ratio. We used the ACORNS pipeline (Brandt et al. 2013) to correct bad pixels, remove correlated read noise, and to correct the field distortion. We did not, however, apply any algorithms to subtract the primary star’s PSF, apart from our removal of an azimuthally symmetric halo. This ensures that there is almost no self-subtraction of the

companion’s PSF. Our goal is to obtain precise relative astrometry and photometry, not to search for very faint companions.

We used only the H -band observations listed in Table 1 to measure relative astrometry, as HiCIAO’s distortion correction is best-characterized in this band. We compute the distortion correction of the HiCIAO camera using images of the dense cores of the globular clusters M5 and M15 (Brandt et al. 2013). We then compare the HiCIAO images of M5 or M15 with the archival M5 or M15 images obtained by *Hubble Space Telescope* and Advanced Camera for Surveys (ACS). The distortion, plate scale, and true north of ACS have been well calibrated (cf. Anderson 2006; Anderson & King 2004; van der Marel et al. 2007). With good seeing, the fractional uncertainties on the distortion are $\sim 10^{-4}$ near the center of the field. The nonlinear component of the distortion is extremely stable between observing runs, with nearly all of the variation confined to the plate scale. We therefore adopt our nonlinear distortion corrections from runs with good observing conditions.

In the case of 2012 November 5, the seeing was poor, so we used observations of M15 from that date to compute the plate scale and use the high-quality 2011 May distortion map for nonlinear-distortion correction. Likewise, for the 2013 January run, we corrected for only the plate scale based on the M5 data that were acquired in the same run, and the nonlinear distortions were corrected using the 2011 May distortion map. HiCIAO’s Lyot stop was replaced before the 2013 October run to improve throughput and angular resolution, necessitating a new measurement of the distortion correction. In the 2013 October and 2015 January runs, we observed globular clusters for the distortion corrections. High-quality data of M5 are available for 2015 January run. Unfortunately, the observing conditions for the 2013 October M15 calibrations were too poor to permit a good measurement of the plate scale and the other distortion components. For this data set we instead used observations of M15 taken in 2013 November, and added an additional uncertainty of 0.25% to the plate scale, corresponding to the measured run-to-run scatter. We find that the new Lyot stop, installed in September 2013, significantly affected HiCIAO’s PSF but had a negligible impact on distortion correction.

After correcting field distortion, we measured the PSF centroids of the primary star on each individual frame by fitting elliptical Gaussians. Then, all the frames from a given observing night were shifted to a common center. Next, the radial profile of the primary star’s PSF was subtracted from each data frame to remove the PSF halo. Failing to remove the PSF halo would bias our measurements both of the companion’s flux and position, as the halo’s mean and gradient are both nonzero at the location of V450 And B. We injected artificial point sources to determine any loss of companion flux due to halo subtraction. We applied these correction factors, though they are mostly very small ($\ll 10\%$). Spatial variations in the Strehl ratio are negligible at the $0''.5$ separation of the binary, while HiCIAO’s flat-field images are stable to $\sim 2\%$ over a period of years (Brandt et al. 2013), smaller than all of our derived photometric uncertainties. Because our data were obtained with the image rotator

TABLE 1
OBSERVING LOG FOR UNSATURATED DATA

Obs. Date (UT)	N_{exp}	t_{tot} (s)	Filter	Mean Airmass	Field Rotation (deg)		Δmag
					Total	Average	
2012 Nov 05	10	100	<i>J</i>	1.09	1.0	0.12	4.23 ± 0.07
–	25	125	<i>H</i>	1.13	24	0.054	4.10 ± 0.05
–	10	50	<i>K_s</i>	1.09	0.66	0.073	3.85 ± 0.07
2013 Jan 02	16	40	<i>J</i>	1.39	0.96	0.024	4.18 ± 0.08
–	7	62	<i>H</i>	1.43	0.60	0.044	3.95 ± 0.06
–	16	24	<i>K_s</i>	1.42	0.74	0.020	3.82 ± 0.08
2013 Oct 16	13	195	<i>H</i>	2.19	1.0	0.062	4.05 ± 0.04
2015 Jan 08	50	575	<i>H</i>	1.08	51	0.10	4.03 ± 0.03

Note: The data sets shown in this table were obtained without a focal-plane mask but with a Lyot stop in a pupil plane (see Section 3). The average field rotation corresponds to the average of each rotation angle during an exposure. Sequences of unsaturated images were taken alternately with saturated frames.

maintaining the orientation of the PSF (ADI mode), the PSF-subtracted frames were de-rotated to align their y axes to celestial north. Finally, the de-rotated frames were combined into a single final frame. We fit an elliptical Gaussian to measure the centroid of V450 And B in this final, halo-subtracted frame; Table 2 lists the relative astrometry for each epoch. Figure 1 shows the final image for the observations at 2015-01-08 without subtracting the radial profile of V450 And A. Note that our analyses for the companion V450 And B are all based on the images with subtracted PSF halos.

To derive the flux ratio between the components, we compare the photometry of the central star and the companion in the same final, combined image. As described above, we measure the companion flux after subtracting the central star’s halo and applying a small correction for flux loss. In order to estimate the error in our measured contrasts, the final image is first convolved with a circular aperture having a radius equal to the full width at half maximum (FWHM) of the PSF. As in Brandt et al. (2013), we use the convolved image and compute the standard deviation of residual signals in an annulus surrounding the central star at the same separation as the companion. This scatter is much larger than the companion’s photon noise.

Our four data sets obtained over three nights contain a small number of pixels with significant ($>3\%$) nonlinearity. Removing frames with one or more pixels above this nonlinearity threshold has a negligible effect on our results, apart from a 0.04 mag difference in photometry for the 2013 January *H*-band observations. We do not exclude these frames when deriving our final photometry (Table 1) and astrometry (Table 2).

3.3. Astrometry Error Analysis

Our error budget for astrometry is dominated by errors in fitting elliptical Gaussians and in determining the plate scale, with lesser contributions from uncertainties in the nonlinear image distortion and from differential atmospheric refraction. We evaluate the uncertainties in the distortion correction using a Markov Chain Monte Carlo (MCMC) method to sample the space of coefficients in the distortion correction polynomial (see Brandt et al. 2013). Where good images of a dense star cluster are available (as for the 2015 January run), the resulting separation errors are negligible ($\lesssim 0.1$ mas). For some runs, however, simultaneous calibration data are

unavailable or are of poor quality. In these cases, we use the 2011 May calibration for the nonlinear distortion and for the orientation of true north. We estimate the resulting uncertainty using the scatter among other runs with good calibration data. The scatter due to the nonlinear distortion is negligible along the vertical axis of the detector, but ranges from $\lesssim 0.1$ mas up to ~ 0.3 mas along the horizontal axis depending on the location in the image where the star is observed. The scatter in the angle of true north is negligible, $0^\circ.031$ (5×10^{-4} rad).

For all but the 2013 October run, we measured the plate scale and its uncertainty using MCMC on simultaneous calibration images. The resulting uncertainties are very small, $\lesssim 0.16$ mas at a separation $0''.5$. The 2013 October run lacks simultaneous calibration data, so we used the full distortion correction measured in 2013 November. We note that a plate scale variation between each run contributes to an astrometric uncertainty. We estimate the resulting astrometric uncertainty from the plate scale to be a non-negligible ~ 1.1 mas by computing the plate scale scatter among 15 other runs with identical instrument configurations (see above for an uncertainty due to the variation of nonlinear distortions).

Finally, we determine the centroid error by calculating the scatter of star-companion separations among sets of frames in an imaging sequence. Before calculating the scatter, all the individual PSF-subtracted frames for a run were divided into several groups and the data in each group were combined. We omitted this step for 2013 January 2 since we have just seven frames, and directly calculated the scatter of separations among those seven frames. The scatter in astrometry among groups of frames ranges from 0.03 to 0.12 pixels (0.3 to 1.1 mas). This is larger than the field distortion errors for all but the 2013 October run, for which simultaneous distortion data were unavailable. We do not independently incorporate an error of the primary star’s centroid into the total error budget. Instead this error is inserted into the astrometry error by computing a scatter of separation measurements between the primary and secondary. This flows from the fact that scatter of the primary star’s centroids result in a scatter of measurements of the primary-secondary separations.

We took all our data with the ADC (Egner et al. 2010) in place. This set of prisms corrects the dependence of the PSF center on wavelength, removing the systematic shift in centroid due to difference in spectral type. Atmo-

TABLE 2
ASTROMETRIC MEASUREMENTS

Obs. Date (UT)	MJD (days)	Separation Angle (mas)	Position Angle ($^{\circ}$)
2012 Nov 05	56236.342	437.87 ± 0.38	73.095 ± 0.062
2013 Jan 02	56294.375	437.5 ± 1.2	71.76 ± 0.17
2013 Oct 16	56581.652	$432.7^a \pm 1.2$	$65.512^a \pm 0.089$
2015 Jan 08	57030.244	422.93 ± 0.43	55.61 ± 0.055

^a Corrected for the effect of atmospheric refraction. The separation and position angle before the correction are 432.3 mas and 65 $^{\circ}$ 520, respectively.

spheric refraction also shifts PSF centroids over the field-of-view. This effect is negligible (< 0.1 mas) for all but the 2013 October observations, which were conducted at airmass 2.19. In that case, we computed the index of refraction as in Mathar (2004, 2007), taking into account the weather conditions during observations: outside atmospheric pressure of 616.3 hPa, outside temperature of 273.19 K, and humidity of 46 percent, as given in the CFHT weather archive³¹. We then corrected the astrometry using a somewhat simplified version of the approach described in Helminiak (2009). A correction of ~ 0.4 mas was applied to the relative separation, while -0.008 was applied to the position angle. We have added these offsets to our astrometry, but note that they are smaller than the astrometric uncertainties. The error bar for each astrometry in Table 2 includes the uncertainties of centroiding, plate scale, angle of true north, and non-linear distortions.

3.4. Archival Spectra and Radial Velocities

The complete set of archival spectra and RV measurements consists of 80 observations coming from three instruments. The total time span of the data is over 18 years, which nearly covers the full orbital period. We present them in Table 7 in the Appendix.

3.4.1. ELODIE

The ELODIE spectrograph is the decommissioned instrument that was attached to the 1.9-m telescope in the Observatoire de Haute-Provence (OHP) in France. From the public ELODIE archive (Moultaka et al. 2004)³² we extracted 25 RV measurements, including six previously unpublished by P03. The total time span is 2536 days (1998 January 8 to 2004 December 18). With one exception, the exposure time varied between 600 and 1200 s; for the majority of observations it was 900 s. The signal-to-noise ratio (SNR) varied from 50 to 116. In one case the exposure time was only 90 s, with a corresponding SNR of 29. The majority of spectra were taken in the simultaneous object-calibration mode (OBTHs), designed for higher RV precision. Two spectra were taken in a different, less precise mode (OBJOs). We took the RV measurements that are directly listed in the archive, and which are given with the precision of 10 m s^{-1} . We recalculated some of the RVs by ourselves (using cross-correlation technique) and found that this precision is sufficient in this case, especially taking into account the systematics and the jitter originating from

the stellar activity (see further Sections). We also calculated the photon-noise RV errors using the formula from Baranne et al. (1996). Following Soubiran et al. (2013), we added in quadrature a systematic RV uncertainty of 15 m s^{-1} for OBTHs observations, and 30 m s^{-1} for OBJOs.

3.4.2. SOPHIE

In the public SOPHIE archive³³ we found another 25 spectra, taken between 2013 September 26 and 2016 February 29 (time span: 886 days). The SOPHIE spectrograph is the current instrument of the OHP 1.9-m telescope. SOPHIE observations were done twice, sometimes three times per night, and the RVs are much more precise than that of the ELODIE data. It is notable that the archive lists different values of velocities than are given in the available CCF headers. We have checked that the latter are more reliable. We have also extracted values of the bisector span, as well as the processed 1D spectra, which we later used for spectral analysis. The exposure times varied from 600 (majority of the spectra) to 900 seconds, and the SNR from 70 to even 190 in one case. Following Soubiran et al. (2013), we added in quadrature a systematic RV uncertainty of 4 m s^{-1} to all the photon-noise uncertainties, which we took directly from the archive.

3.4.3. Hamilton

Recently, Fischer et al. (2014) published measurements of the Lick planet search program, carried out using the Hamilton spectrograph at the 3.5-m Shane telescope in the Lick observatory in California. Available are 30 data points spanning 5012 days (1998 January 18 to 2011 October 9), which is the longest time span of all the data sets we used. It also covers the gap between ELODIE and SOPHIE observations, which was crucial for merging all the data in the orbital fit. Contrary to SOPHIE and ELODIE, the Hamilton measurements are not given for the instrument's zero-point, but instead are shifted, so their average is 0. The SNR of the spectra varies from 60 to 200, in most cases exceeding 100. Exposure times are not given.

3.5. Hipparcos Photometry

V450 And is a BY Dra-type variable, and the photometric variability is likely related to the presence of spots on the rotating disk of the star, so its period represents the period of rotation. Unfortunately, the value of 7.6 d given in Strassmeier et al. (2000) is marked as uncertain. A value of 7 d can also be found in the literature (Isaacson & Fischer 2010), but it was found from period-activity relations, not measured directly, and we also find it unreliable.

In order to assess the rotation period we took the *Hipparcos* time-series photometry (Perryman et al. 1997) and ran a Lomb-Scargle periodogram³⁴. We focused on periods between 2 and 50 days, and set the constant step in frequency of $1/10W \simeq 9.13 \times 10^{-5} \text{ d}^{-1}$, where

³³ <http://atlas.obs-hp.fr/sophie/>

³⁴ Periodograms for this work were created with the on-line NASA Exoplanet Archive Periodogram Service: <http://exoplanetarchive.ipac.caltech.edu/cgi-bin/Pgram/nph-pgram>

³¹ <http://mkwc.ifa.hawaii.edu/archive/wx/cfht/>

³² <http://atlas.obs-hp.fr/elodie/>

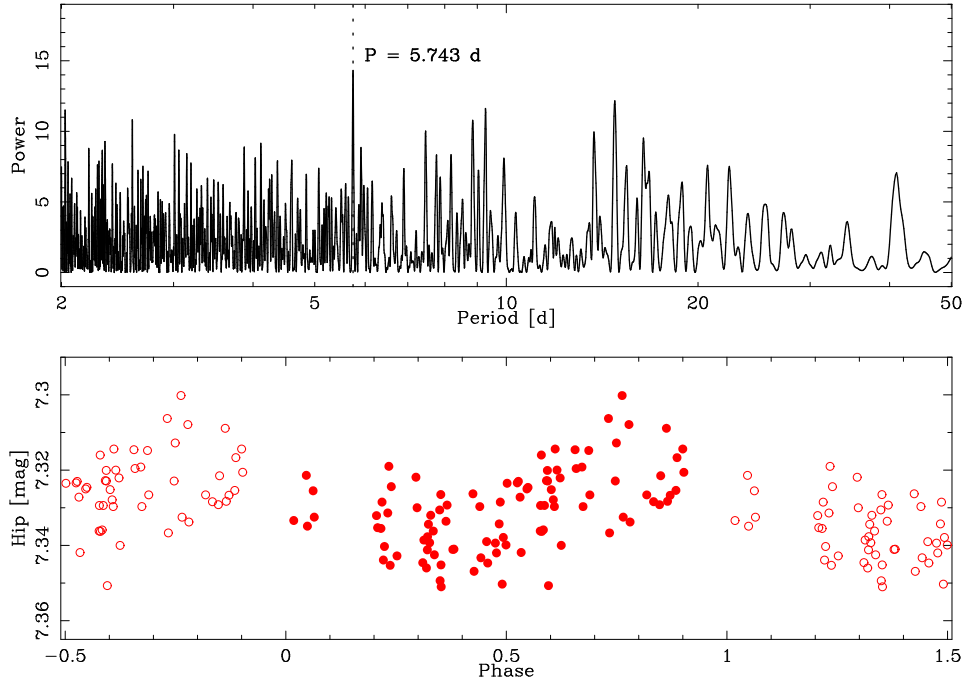


FIG. 2.— *Top*: The Lomb-Scargle periodogram of the *Hipparcos* photometry, with the most distinct peak at $P = 5.743$ d marked. *Bottom*: The *Hipparcos* data phase-folded with the 5.743 d period. For clearance, we replot the data with open symbols for phases < 0 and > 1 .

$W \simeq 1096$ d is the time span of *Hipparcos* data. The most distinct peak is found at $P = 5.743 \pm 0.003$ d or $f = 0.17411(91)$ d $^{-1}$. The periodogram and *Hipparcos* data phase-folded with this period are shown in Figure 2.

4. ORBITAL SOLUTION

Both the radial velocity and astrometry data were fit simultaneously with a Keplerian model to solve for the system’s orbital parameters. The full solution includes 9 parameters, with a further 3 for the spectrograph offsets. To perform the fitting, we adopt a Bayesian approach similar to that discussed in Ford (2006). The posterior probability distributions for the model parameters are proportional to the product of the model parameter’s likelihood, $\mathcal{L}(\text{Model})$, and their prior probability based on previous knowledge, $p(\text{Model})$. Assuming the data errors (σ) are independent and follow a Gaussian distribution, the likelihood may be written as

$$\mathcal{L}(\text{Model}) = \exp\left(-\frac{\chi^2}{2}\right) \quad (1)$$

with

$$\chi^2 = \sum_i \frac{(\text{Model}_i - \text{Data}_i)^2}{\sigma_i^2}, \quad (2)$$

and the priors used in our model fitting are summarized in Table 3.

Our Keplerian model includes the directly varied parameters: m_1 , m_2 , e , P , ϖ , T_0 , i , Ω , ω , γ_1 , γ_2 , γ_3 ; respectively these are, the mass of the primary star, mass of companion, eccentricity, period, parallax, time of last periastris, inclination, longitude of the ascending node, argument of periastris, and the radial velocity offsets for each spectrograph (ELODIE, Hamilton and SOPHIE). Including the parallax as a varied parameter ensures its estimated errors and prior probability distributions are

TABLE 3
ADOPTED BAYESIAN PRIORS

Parameter	Prior
ϖ	Gaussian ^a $\times (1/\varpi^4)$
e	$p(e) \propto e^b$
P	Logarithmic
i	$p(i) \propto \sin(i)$
m_1 & m_2	PDMF ^c
others	Uniform

^a *Hipparcos* value of 37.25 ± 0.55 mas, from van Leeuwen (2007)

^b From Duquennoy & Mayor (1991)

^c Present-Day Mass Function (Chabrier 2003, Table 1)

appropriately included into the posteriors. Fitting these 12 parameters with a direct sampling approach, such as simple Monte Carlo, can be difficult due to their possibly complicated likelihood topography. To overcome this we use the Markov Chain Monte Carlo (MCMC) features of a new software package entitled the Exoplanet Simple Orbit Fitting Toolbox (ExoSOFT; K. Mede & T. Brandt 2016, in preparation). This toolbox explores the parameter space using a multi-stage approach ending in MCMC. It is capable of fitting any combination of astrometry and radial velocity data, and performs automated post-processing to summarize the results. The code was written primarily in the Python programming language with the computationally intensive model in C++.

Prior to utilizing both forms of observational data, initial fits were performed with only the radial velocity data. During this, an instrument-independent jitter was added in quadrature with the estimated RV uncertainties, and adjusted until a value of 13.6 m s^{-1} produced a best reduced $\chi^2 = 1$. Following this step, a full joint analysis

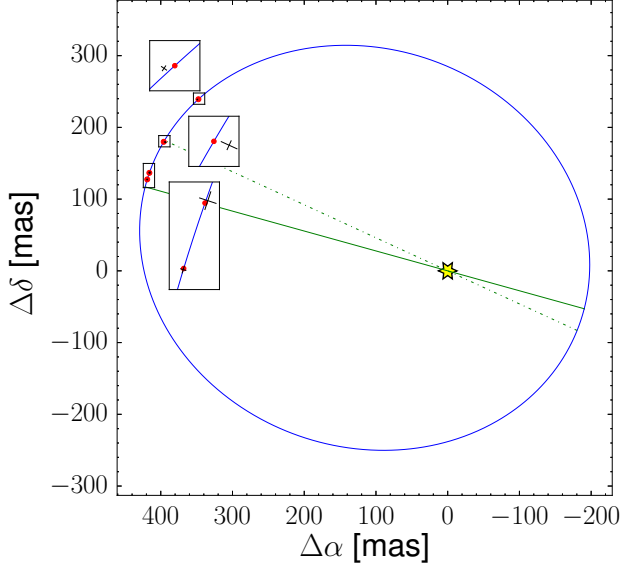


FIG. 3.— Astrometric orbit of V450 And B relative to A (marked as yellow star). The line of apsides and line of nodes are marked with the solid and dotted green lines, respectively. Our HiCIAO measurements are shown as black crosses to indicate the astrometric errors; the insets are magnified by a factor of ten.

was performed to find the posterior probability distributions of the orbital parameters. Figures 3 and 4 show the best fit orbit in both astrometry and RV. Table 4 summarizes both the best-fitting and median values, as they differ due to asymmetries in the posterior distributions. For the MCMC stage we ran 7 parallel chains of 2×10^8 samples each to achieve sufficient convergence to the posteriors, shown in Figure 5, measured by a Gelman-Rubin statistic value of 1.0006.

We found that the secondary is a $0.279^{+0.023}_{-0.020}$ M_{\odot} star (suggesting it is an M dwarf) on a nearly face-on, eccentric orbit. The orbital period of 21 years is over two times longer than suggested in P03, which is mainly due to the much shorter time span of their data (~ 4.5 years), which led to a poor determination of orbital parameters. The resulting $m_2 \sin(i)$ is therefore much larger than in P03, and the companion cannot be a brown dwarf. We were a bit fortunate that our imaging covered the apocenter passage. The orbital parameters are given with a very good precision (e.g.: 0.53% in K), mainly thanks to the almost complete (87%) coverage of the orbit with RV data, despite the stellar activity. The near face-on orientation of the orbit adds to the difficulty in determining the companion mass, therefore our $0.277^{+0.024}_{-0.019}$ M_{\odot} median fit for m_2 has $\sim 10\%$ error. These values arise from our choice to make both the primary star’s mass and the parallax directly varied parameters, ensuring their errors are appropriately handled at every step in the MCMC chains and the resulting posterior distributions.

As shown in Figure 6, the posterior probability distributions for the masses m_1 and m_2 are anti-correlated. This is largely due to Kepler’s third law:

$$a_{\text{total}} = \left[\frac{P^2 G (m_{\text{total}})}{4\pi^2} \right]^{1/3} \quad (3)$$

As listed in Table 4, both the a_{total} and P fits are at

TABLE 4
RESULTS OF THE JOINT ASTROMETRIC+RV KEPLERIAN ORBITAL FIT.

Parameter	Best-fit	Median	68% range ^a
m_1 (M_{\odot})	1.141	1.113	(1.049:1.178)
m_2 (M_{\odot})	0.279	0.277	(0.259:0.301)
ϖ (mas)	37.24	37.34	(36.79:37.89)
e ()	0.3781	0.3795	(0.3759:0.3831)
T_0 (JD-2452302)	41.7	46.8	(37.0:56.5)
P (yr)	20.960	20.044	(20.983:21.109)
i ($^{\circ}$)	160.4	160.5	(159.0:162.2)
Ω_2 ($^{\circ}$)	245.27	245.14	(244.61:245.67)
ω_2 ($^{\circ}$)	350.22	350.58	(349.96:351.19)
a_{total} (AU)	8.54	8.51	(8.38:8.64)
K (m s^{-1})	864.8	865.5	(861.0:870.1)
γ_{ELO} (m s^{-1}) ^b	6262	6267	(6261:6273)
γ_{Ham} (m s^{-1}) ^b	381.7	384.0	(379.4:389.7)
γ_{SOP} (m s^{-1}) ^b	6322	6322	(6316:6328)
χ^2 (ν) ^c	83.87 (76)

^a Approximate 1σ uncertainty: 68.3% of the posterior probability lies in this range.

^b Radial velocity offsets: systemic velocities for ELODIE and SOPHIE, difference between the average and systemic velocity for Hamilton.

^c ν represents the number of degrees of freedom during MCMC joint fitting $\nu = (4 \text{ DI epochs})(2 \text{ dimensions}) + (80 \text{ RV epochs})(1 \text{ dimension}) - (12 \text{ varied params}) = 88 - 12 = 76$ dof.

least ~ 4 times tighter than for the masses. Equation (3) requires that the total mass ($m_{\text{total}} = m_1 + m_2$) must also have a relatively narrow distribution, even after taking the cube of a_{total} .

5. SPECTRAL ANALYSIS

The literature values of atmospheric parameters of V450 And, such as the effective temperature T_{eff} , metallicity $[M/H]$, or logarithm of gravity $\log(g)$, are not always in agreement with each other. Temperatures vary from 5546 (Holmberg et al. 2009) to 5755 K (Valenti & Fischer 2005), $\log g$ from 4.35 (Gray et al. 2003) to 4.60 (Takeda et al. 2007), and the metallicity from -0.30 (Holmberg et al. 2009) up to +0.07 dex (Kovtyukh et al. 2004). As our intention was to compare our results with theoretical models and obtain as complete description of the system as possible, we decided to perform our own spectral analysis, based on the SOPHIE spectra. We used the freely available, python-based software iSpec (Blanco-Cuaresma et al. 2014)³⁵, that compares an observed spectrum with a number of synthetic ones generated on-the-fly, and uses a least-squares minimization algorithm. We first fit the continuum, but we cropped all the spectra at 4000 Å, because the wide calcium H and K lines, and poor SNR in the blue part, make the continuum fitting difficult for shorter wavelengths. No errors were assigned to the (relative) fluxes. We also corrected all the spectra for their barycentric velocity. We set the spectral resolution to 75000 (as in the instrument’s specifications), and fitted for the temperature, metallicity, $\log(g)$ and projected rotational velocity $v \sin(i)$. Following Valenti & Fischer (2005), we set the microturbulence velocity v_{mic} to 0.85 km s^{-1} , and for the macroturbulence velocity v_{mac} we adopted their Equation (1), assuming $T_{\text{eff}} = 5700 \text{ K}$, which gives

³⁵ <https://www.blancocuaresma.com/s/iSpec/>

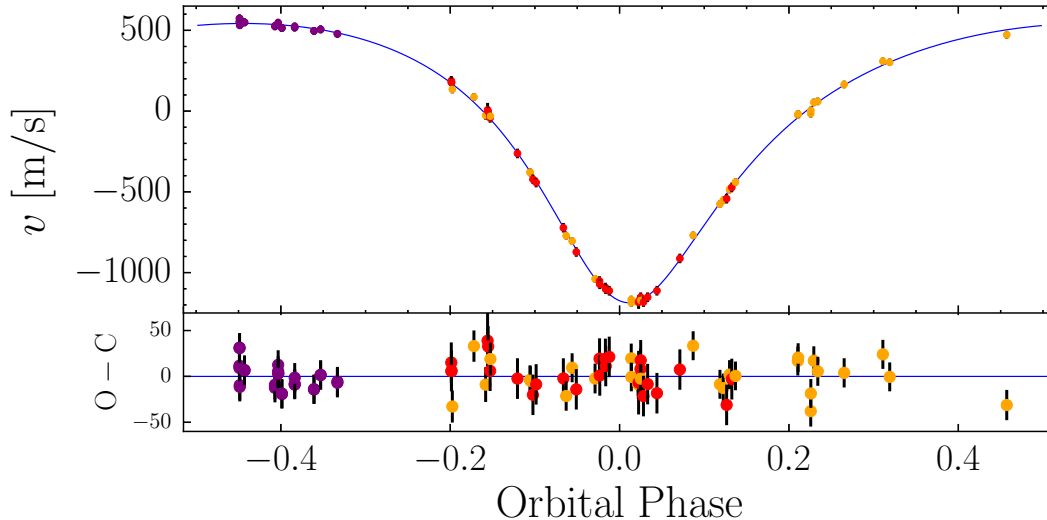


FIG. 4.— Radial velocity measurements from ELODIE (red), Hamilton (orange) and SOPHIE (purple) observations, and the fitted RV curve of V450 And A, phase-folded with the orbital period. Measurements are shifted by the values of offsets given in Table 4. The lower panel shows the residuals of the fit. The jitter is included in the error bars; they are plotted in the upper panel as well, but cannot be seen there as they are comparable to the size of the points.

TABLE 5
RESULTS OF THE I SPEC SPECTRAL ANALYSIS

Parameter	Weigh.Avg.	\pm	<i>rms</i>	Mean ind.err.
T_{eff} (K)	5721	5	27	107
$\log(g)$ (cm s^{-2})	4.44	0.02	0.07	0.16
$[M/H]$ (dex)	0.038	0.005	0.027	0.067
$v \sin(i)$ (km s^{-1})	4.02	0.07	0.34	0.55

$v_{\text{mac}} = 3.87 \text{ km s}^{-1}$. The relation predicts a change in v_{mac} by 1 km s^{-1} per 650 K, so we conclude that the systematic uncertainty of the fitted parameters, coming from incorrect temperature we assumed, is negligible. We performed a number of tests, running iSpec on spectra of several stars with well-constrained parameters, provided together with the iSpec itself, or by the *Gaia*-ESO survey. We found that the consistency with the reference values is the best when iSpec uses the MARCS GES atmosphere models (Gustafsson et al. 2008), solar abundances from Grevesse et al. (2007), and VALD atomic lines (Kupka et al. 2011).

The iSpec was run on each SOPHIE spectrum separately. Individual results derived from each spectrum were then weight-averaged, and these values are given in Table 5. They are all within the ranges of values found in the literature. The errors for the weight-averaged results are indicated by “ \pm ”, and the *rms* of all individual results are also provided in Table 5. Errors of the individual iSpec results were larger than the *rms*. For each parameter we also give the mean of the individual errors.

6. DISCUSSION

6.1. Activity and Rotation

As a BY Dra type variable, V450 And has been known to show some level of activity. Emission in Ca II H and K lines has been noted, (Strassmeier et al. 2000; Gray et al. 2003; Wright et al. 2004; Isaacson & Fischer 2010), and a photometric variability of 0.02 mag has also been reported (Strassmeier et al. 2000). In Section 3.5 we de-

scribed how the period of rotation (5.743 d) has been found. The same period can be seen in SOPHIE radial velocities, i.e. in the residuals ($O - C$) of the orbital fit. In Figure 7 we present them as a function of the rotation phase, and the bisector span *bis*. The correlation between *bis* and ($O - C$) proves the activity origin of the observed RV modulation. The activity of V450 And A mimics a $0.14 M_J$ planet on an eccentric orbit – a pseudo-orbital fit to all the residuals is also shown, with an *rms* of only $\sim 8 \text{ m s}^{-1}$. We would like to note that we did not model the activity-related RV variations together with the orbital motion due to two reasons. First, only the SOPHIE data are precise enough to see it clearly, and they do not cover a substantial part of the orbit. Second, we suspect that the pattern of spots (and thus the RV modulation they produce) evolves in time. When making the pseudo-orbital fit to residuals from only one season, one can lower the *rms* to 2-3 m s^{-1} , and for each season obtain different parameters (shape) of the pseudo-orbit (different e, K, ω , etc.).

In the further analysis we thus assumed 5.743 d to be the period of rotation. Taking the best-fitting dynamical mass of the star, and $\log(g)$ from the spectral analysis, we can estimate the radius of V450 And A to be $1.09^{+0.09}_{-0.11} R_{\odot}$. This value of radius, the estimated rotational period, and projected velocity of rotation $v \sin(i)$ lead to the rotation inclination angle of 24.8 or $155.2 \pm 5.5^\circ$, which is in agreement with the orbital inclination. Due to a long orbital period and young age (see next Section), we posit that the system formed in this way, rather than was aligned by tidal forces. A nearly pole-on orientation of the component A may also partially explain why the amplitude of photometric variability is only 0.02 mag – if spots are present near the star’s pole, their visibility does not change much with the phase of rotation. Such polar or high-latitude spots have been observed on stars of similar mass, spectral type and rotation period (e.g., Strassmeier & Rice 1998; Sanchis-Ojeda et al. 2013). In addition, theoretical models support this tendency (e.g., Granzer et al. 2000;

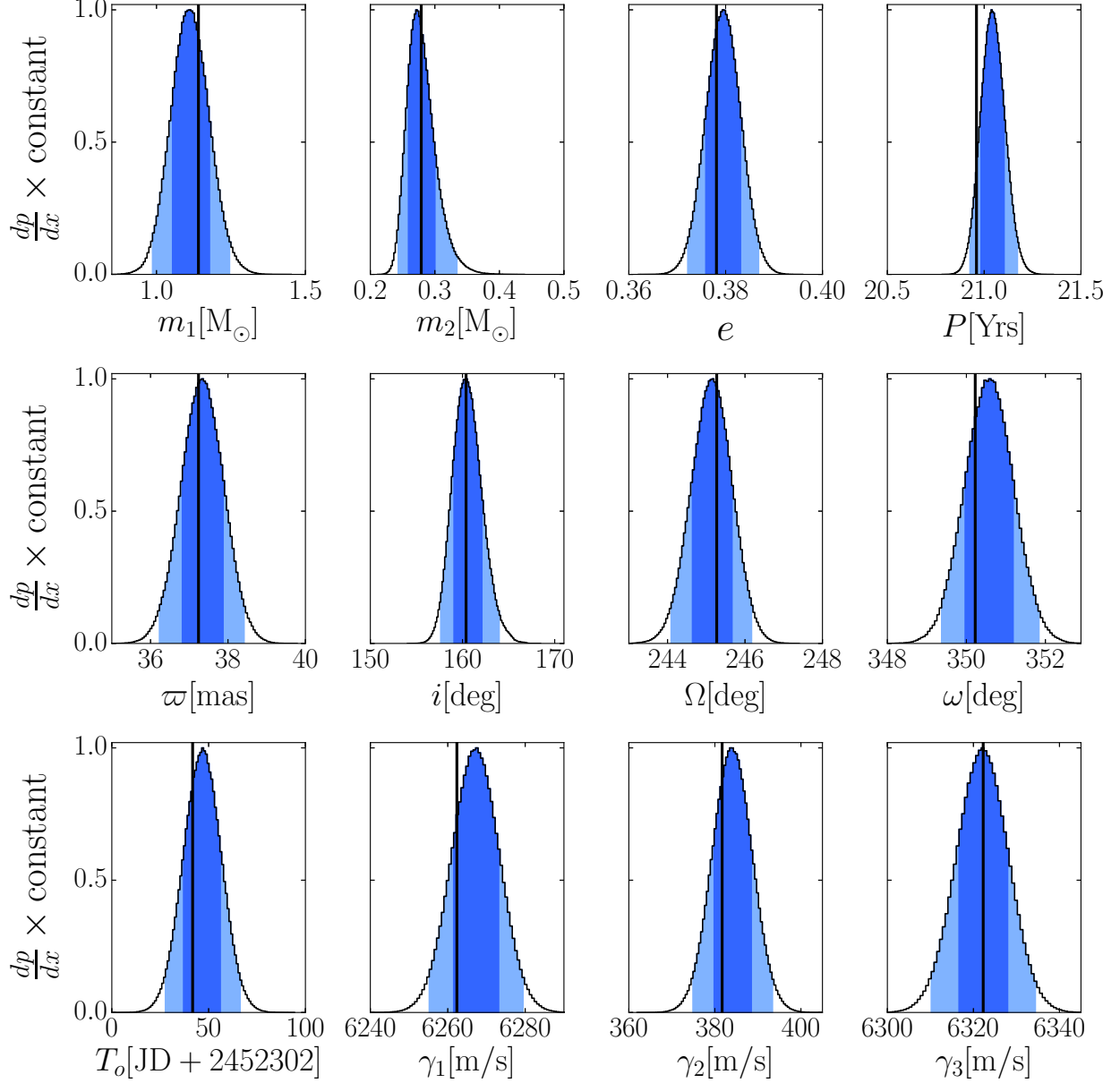


FIG. 5.— The MCMC posterior distributions of the varying parameters. Best-fit values are marked with black vertical lines, while the dark and light blue ranges represent the 68.3 and 95.4% (1 and 2σ) confidence levels, respectively. The consecutive offsets (γ) are for the ELODIE, Hamilton, and SOPHIE instruments.

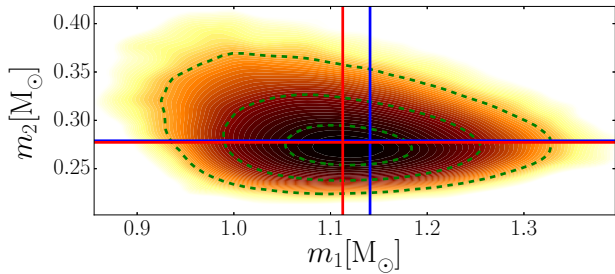


FIG. 6.— A 2-dimensional density plot for comparison of the final posterior density function for m_1 and m_2 . Dashed contours indicate the 3σ , 2σ , and 1σ confidence levels, with the best fit and median values as solid blue and red lines.

Yadav et al. 2015). Hence, it is likely that we observed

spots near the star's pole, systematically affecting our luminosity and temperature estimates for V450 And A (see Section 6.3).

6.2. Age from Activity and Gyrochronology

Stars with convective envelopes generate magnetic fields that couple them to their stellar winds. The stars shed angular momentum, spinning down and becoming less active with time (Skumanich 1972). This spindown, either measured directly through a rotation period or indirectly through coronal and chromospheric activity, can be used to date cool main sequence stars (Barnes 2003). The decline of rotation and activity has been calibrated using clusters and binaries to enable gyrochronology (Barnes 2007; Mamajek & Hillenbrand 2008).

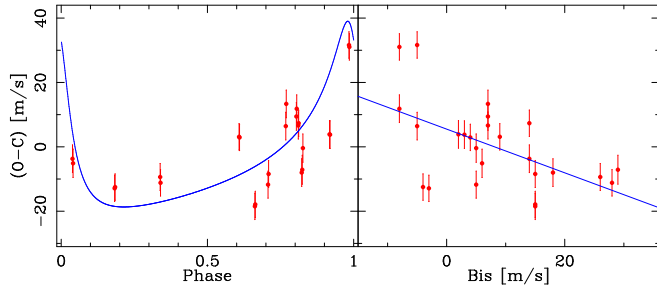


FIG. 7.— *Left*: SOPHIE residuals of the orbital fit phase-folded with the period of rotation. The blue line shows a pseudo-orbital fit to these residuals, that mimics a $0.14 M_J$ planet on an $e = 0.62$ orbit. *Right*: The same residuals shown as a function of bisector span. The blue line shows a linear fit, and the correlation coefficient is -0.602 . The vertical error bars on both panels are the RV measurement errors that we used in our analysis before adding the jitter.

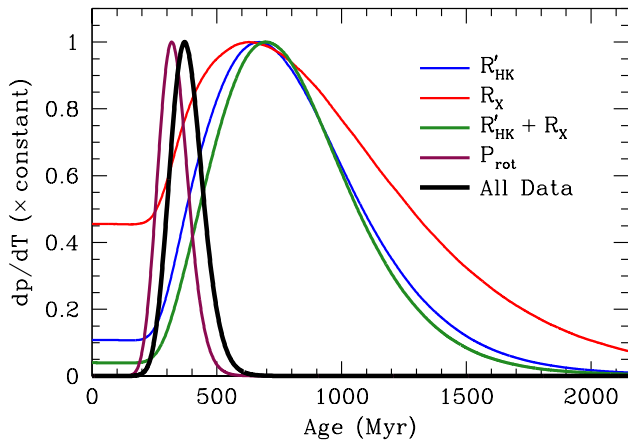


FIG. 8.— Posterior probability distributions of the age of V450 And from its rotation and activity indicators, using the method described in Brandt et al. (2014). There is a modest tension between the age estimated from chromospheric activity and that inferred from rotation; our rotation period dominates the total posterior probability distribution.

V450 And A's $B - V$ was measured by Tycho-2 (Høg et al. 2000) and we convert that to the Johnson $B - V$ ($= 0.690 \pm 0.015$), which is adopted in the following analysis. V450 And has well-measured rotation and activity indicators, including the period of 5.7 days derived in the preceding section, a *ROSAT* X-ray flux (Voges et al. 1999), and Ca II HK chromospheric activity measurements. We use the bolometric corrections of Flower (1996) as corrected by Torres (2010) to convert the measured X-ray flux into R_X , the ratio of X-ray to bolometric flux; we obtain $\log_{10} R_X = -4.65$. From Pace (2013), there are 29 literature measurements of the Ca II HK S index, ranging from 0.235 to 0.348. The lowest measured value, from White et al. (2007), is a clear outlier, while the single measurement from Strassmeier et al. (2000) must be calibrated to the Mount Wilson system. The remaining 27 measurements, from Gray et al. (2003), Wright et al. (2004), and Isaacson & Fischer (2010), have a mean of 0.324 and a standard deviation of 0.013. The median of all literature measurements is an indistinguishable 0.322; we adopt this value as our Ca II HK index and convert it to $\log_{10} R'_{HK} = -4.48$ using the formulae given

TABLE 6
ABSOLUTE JHK MAGNITUDES OF V450 AND

	Primary	Secondary
M_J (mag)	3.822 ± 0.037	8.002 ± 0.086
M_H (mag)	3.530 ± 0.041	7.581 ± 0.044
M_{K_s} (mag)	3.455 ± 0.039	7.275 ± 0.088

in Noyes et al. (1984).

We adopt the approach of Brandt et al. (2014) to obtain a posterior probability distribution on the age of V450 And from its rotation and activity. Brandt et al. (2014) used the calibrated relations of Mamajek & Hillenbrand (2008), but also accounted for the fact that stars spend a variable amount of time as rapid rotators before they begin to spin down in earnest (Barnes 2007). For a $\sim 1 M_\odot$ star, Brandt et al. (2014) assumed an additional spin-down time uniformly distributed between 0 and ~ 150 Myr, effectively broadening the posterior probability distributions.

Figure 8 shows the ages as inferred from the method of Brandt et al. (2014) using the rotation and activity indicators individually, and by combining all age indicators. We obtain a final age estimate of 380^{+220}_{-100} Myr, (at 90% confidence). There is a mild tension between the age preferred by chromospheric activity (300–1800 Myr) and that favored by our measured rotation period, which dominates our posterior probability distribution. Following Brandt et al. (2014), we include a 5% probability that the star's rotation and activity do not reflect its true age and that the star could be at any point on its main sequence evolution.

6.3. Comparison with Models

In order to estimate the age of the system on the basis of theoretical stellar evolution models, we compared our results with the Baraffe et al. (2015, hereafter BHAC15) and Padova-TRIESTE Stellar Evolution Code (PARSEC; Bressan et al. 2012; Chen et al. 2014) isochrones. The former set is calculated only for the solar composition, but our iSpec analysis gives metallicity very similar to solar. For PARSEC we used our value of $[M/H]$, which translates into $Z = 0.0166$ in this set. We checked and confirmed that using the solar composition ($Z = 0.0152$) does not change the final results significantly, so the usage of $[M/H] = 0.0$ BHAC15 models is justified.

For the comparison we use our estimates of dynamical masses and absolute JHK_s magnitudes, as they are the most robust parameters we can obtain from our observations for both components. To compute the absolute magnitudes, we assumed the *Hipparcos* distance to the system, and took the total apparent brightnesses of the system and our magnitude differences from HiCIAO. We list the absolute magnitudes in Table 6. The results are shown in Figure 9. Errors of the values for both components come mainly from the parallax uncertainty, with a small contribution from the uncertainties of the observed magnitudes. For the secondary only, the second dominant source of errors is the differential photometry from Table 1.

Both sets of models give quite consistent results. The resulting ages are 400^{+2600}_{-250} Myr ($\log(\tau) = 8.60^{+0.88}_{-0.43}$) for

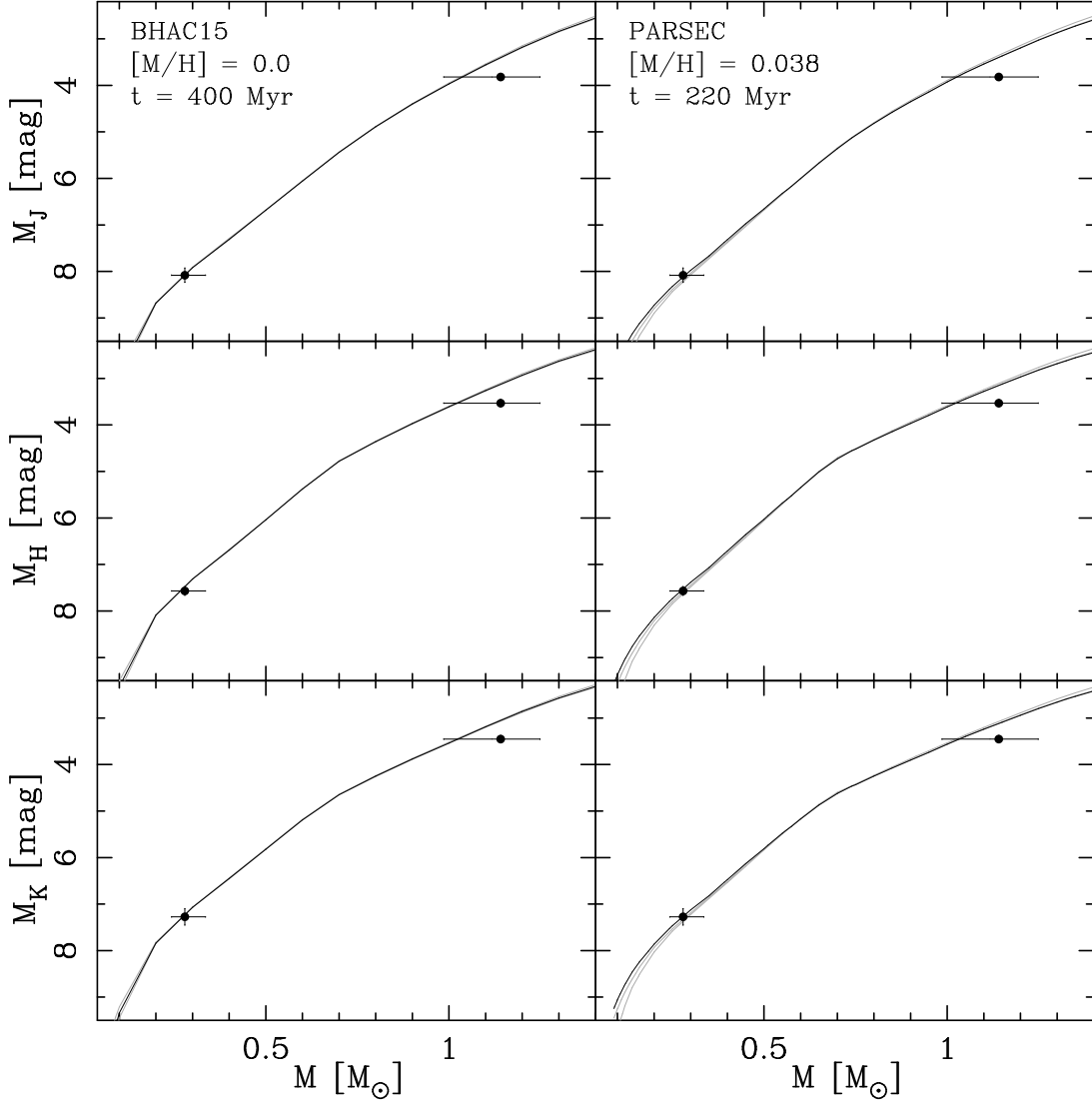


FIG. 9.— Comparison of our results, with 95% confidence level error bars, with theoretical models. The best-fitting isochrones of BHAC15 (400 Myr; left) and PARSEC (220 Myr; right) sets are shown as black lines (J [top], H [middle], K -band [bottom]) on mass vs. absolute magnitude planes. Grey lines are isochrones for ages of 280 and 600 Myr, which are 90% confidence limits from Section 6.2. Assumed metallicities are labeled for each set.

BHAC15, and 220^{+2120}_{-90} Myr ($\log(\tau) = 8.34^{+1.03}_{-0.22}$) for PARSEC. We adopt the latter because of the smaller error bars. The best-fitting age values are tightly constrained by the best-fitting value of m_2 , as found in the orbital fit. The lower limits are defined by the 95% confidence level of the parameters of the secondary, while the primary analogously defines the upper limits. In other words, isochrones of the given range of ages reside within mass vs. absolute (JHK_s) magnitude planes that are defined by 95% confidence levels (corresponding to $\sim 2\sigma$ for symmetrical posteriors), as derived from both components. The large positive uncertainty is strictly related to the fact that stars do not change much during the main sequence phase, and isochrones for much older years still reside within the error bars shown in Fig. 9.

The primary tends to be systematically too faint for its mass. The PARSEC model, for $\tau = 220$ Myr and $[M/H] = 0.038$, predicts absolute magnitudes lower by 0.92 in U , 0.65 in V , and 0.30 mag in K with respect to observed values -5.94 (Myers et al. 2015), 5.74 (Høg et al. 2000),

and 3.46 mag (Cutri et al. 2003), respectively, as derived from literature data and distance. This is mainly because the effective temperature at the age of ~ 220 Myr is ~ 450 K higher in models than what we found with iSpec. This can be at least partially explained by the presence of polar spots, seen in photometry, which decrease the observed T_{eff} and brightness.

Our analysis also shows that the secondary has just reached the main sequence, but spots may also hamper its results, making it appear fainter. In such a case the true absolute magnitude would be different, and the secondary would move up on Fig. 9.

Ages derived from comparison with both sets of models are in good agreement with results from Section 6.2. In Fig. 9 we also plot isochrones for ages of 280 and 600 Myr, which are the 90% confidence limits of the Brandt et al. (2014) method. With a bit higher temperature of the primary, the agreement would be even better. Additionally, our m_1 determination may be slightly overestimated, due to uncertainties in parallax or astrometry, for example.

Please also note that the median of the m_1 posterior distribution is smaller. Because, as discussed in Section 4, the sum of two masses is fairly well constrained, this would mean that m_2 is higher. Including the possible effect of spots on component B, described above, the secondary would then move on Fig. 9 almost exactly along the isochrone. The resulting age would thus be intact. This issue would be fixed if radial velocities of the secondary were measured directly.

Overall, we obtained a consistent image of the V450 And binary. It is a fairly young, few hundred Myr old system, but with both components already on the main sequence. Probably both stars are active (primary is for sure), and possibly their mass ratio is slightly closer to 1, as compared with the best-fitting value we obtained. Our age estimates, especially from Sect. 6.2, agree well with one of the two mostly accepted determinations of the age of the Castor moving group: 440 ± 40 Myr (Mamajek 2012). The less-agreeing one is 700^{+150}_{-75} Myr (Monnier et al. 2012). However, it was recently suggested by Mamajek et al. (2013) and Zuckerman et al. (2013) that this moving group is actually a collection of kinematically similar stars showing a spread of ages, rather than a well-defined kinematic structure.

7. SUMMARY AND FUTURE PROSPECT

In this work we have presented our analysis of a low-mass companion originally discovered with the RV technique, and since detected with high-contrast imaging. In comparison with previous work by P03, we employ in our analysis additional astrometry and more RV data, covering almost the whole orbital period. This enables us to better constrain the orbit, as well as other crucial systems parameters. We derived the full set of orbital parameters and masses for both components, showing that the secondary is an M-type star, not a brown dwarf as suggested by P03. With the support of the results of our spectral analysis, and the observed activity of the primary, we conclude that the system is still relatively young (~ 200 -400 Myr). The combined RV and imaging data allowed us to draw a full image of the V450 And system.

The presented work may be a test case for future studies, aimed for characterisation of known brown dwarf and exoplanet candidates. Cases like V450 And, HD 16760, or objects from the recent study by Wilson et al. (2016), clearly show the need to support RVs with other kinds of data. With the capabilities of already existing extreme adaptive optics systems, like SCExAO at Subaru (Martinache et al. 2014; Jovanovic et al. 2015), GPI at Gemini (Macintosh et al. 2014) or SPHERE at VLT (Beuzit et al. 2008), and their future generations that will be working with the incoming 30-m class telescopes, it will be possible to detect and directly characterise companions of lower masses and shorter orbital periods than V450 And B. This may bring a revision of our knowledge of long-period brown dwarf and massive planet candi-

dates, their distribution, initial mass function, and mechanisms of their formation, for example by pointing out objects in the “brown dwarf desert” (Marcy & Butler 2000; Grether & Lineweaver 2006; Wilson et al. 2016).

We would like to thank Dr. Rodolfo Smiljanic and Dr. Milena Ratajczak, both from the N. Copernicus Astronomical Center, Poland, for providing the *Gaia*-ESO survey spectra for tests, and for their comments regarding the spectral analysis. We are also grateful to Dr. Roberto Sanchis-Ojeda for a useful discussion, and to David Lafrenière for generously providing the source code for the ADI data reductions.

This work is based in part on data collected at Subaru Telescope, which is operated by the National Astronomical Observatory of Japan. Our data reductions in part were performed with PyRAF and PyFITS, which are products of the Space Telescope Science Institute (STScI/AURA/NASA). Our analysis is also based on observations made with the NASA/ESA Hubble Space Telescope, and obtained from the Hubble Legacy Archive, which is a collaboration between the Space Telescope Science Institute, the Space Telescope European Coordinating Facility (ST-ECF/ESA) and the Canadian Astronomy Data Centre (CADN/NRC/CSA). Data analysis were in part carried out on common use data analysis computer system at the Astronomy Data Center, ADC, of the National Astronomical Observatory of Japan. This research has made use of the VizieR catalogue access tool and the SIMBAD database, which are operated at CDS, Strasbourg, France.

K.G.H. acknowledges support provided by the National Astronomical Observatory of Japan as Subaru Astronomical Research Fellow. M.K. was supported by Japan Society for Promotion of Science (JSPS) Fellowship for Research and this work was partially supported by the Grant-in-Aid for JSPS Fellows (Grant Number 25-8826). K.M. gratefully acknowledges support from the Mitsubishi Corporation International Student Scholarship. This work was performed in part under contract with the Jet Propulsion Laboratory (JPL) funded by NASA through the Sagan Fellowship Program executed by the NASA Exoplanet Science Institute. N.N. acknowledges supports by the NAOJ Fellowship, Inoue Science Research Award, and Grant-in-Aid for Scientific Research (A) (JSPS KAKENHI Grant Number 25247026). J.C.C. was supported by the U.S. National Science Foundation under Award No. 1009203. M.T. is supported by JSPS KAKENHI Grant (Number 15H02063).

Finally, the authors recognize and acknowledge the very significant cultural role and reverence that the summit of Maunakea has always had within the indigenous Hawaiian community. We are most fortunate to have the opportunity to conduct observations from this mountain.

Facilities: Subaru (HiCIAO, AO188), OHP:1.93m (ELODIE, SOPHIE), Shane (Hamilton spectrograph)

APPENDIX

In Table 7 we present all RV measurements used in this study, given in the original form and numerical precision as in the source. For each measurement we also give the final measurement error (including systematics but without the jitter), the value of RV with respect to the offset (RV- γ), residual (O-C), and the instrument that was used.

TABLE 7
RADIAL VELOCITIES OF V450 AND

BJD -2450000	RV \pm err (m s ⁻¹)	RV- γ (m s ⁻¹)	O-C (m s ⁻¹)	Sp. ^a
822.3353812	6380 \pm 15.1	184.0	12.6	E
823.3797985	6370 \pm 15.1	174.0	3.2	E
824.3384884	6370 \pm 15.1	174.0	3.7	E
831.6181600	516.60 \pm 8.12	134.5	-32.1	L
1027.0039100	468.65 \pm 7.30	86.5	33.9	L
1132.8232400	354.28 \pm 10.76	-27.8	-8.0	L
1150.3587309	6170 \pm 30.8	4.0	36.6	E
1155.4064768	6190 \pm 15.5	-6.0	30.4	E
1173.3595108	6150 \pm 15.1	-46.0	3.8	E
1175.7724600	350.44 \pm 8.73	-31.7	19.9	L
1420.6268456	5930 \pm 15.4	-266.0	-4.8	E
1533.8017600	3.94 \pm 4.16	-378.2	-3.1	L
1536.6826200	0.00 \pm 4.09	-382.1	-4.0	L
1560.3601856	5770 \pm 15.2	-426.0	-22.7	E
1589.2844593	5750 \pm 15.2	-446.0	-11.3	E
1835.5565444	5470 \pm 15.1	-726.0	-5.5	E
1860.8232400	-390.08 \pm 4.72	-772.2	-21.5	L
1914.6845700	-423.26 \pm 3.96	-805.4	9.1	L
1952.3257010	5320 \pm 15.2	-876.0	-17.7	E
2121.9785200	-657.11 \pm 5.36	-1039.2	-2.9	L
2162.5770622	5140 \pm 15.4	-1056.0	15.5	E
2164.6197949	5120 \pm 15.2	-1076.0	-2.8	E
2215.4971564	5100 \pm 15.2	-1096.0	15.4	E
2218.5181787	5090 \pm 15.1	-1106.0	7.4	E
2250.3889077	5080 \pm 15.3	-1116.0	17.5	E
2448.9902300	-785.27 \pm 5.19	-1167.4	19.7	L
2449.9845300	-805.42 \pm 3.24	-1187.5	-0.6	L
2509.9082000	-796.22 \pm 2.98	-1178.3	-0.6	L
2512.0263700	-800.46 \pm 3.48	-1182.6	-5.3	L
2513.0146500	-803.54 \pm 3.24	-1185.7	-8.7	L
2515.6315310	5010 \pm 30.1	-1186.0	-9.7	E
2532.6263008	5030 \pm 15.2	-1166.0	5.4	E
2534.6200153	5040 \pm 15.3	-1156.0	14.8	E
2534.9335900	-790.54 \pm 3.77	-1172.7	-2.0	L
2559.6019814	5010 \pm 15.3	-1186.0	-24.1	E
2597.4354178	5040 \pm 15.3	-1156.0	-10.9	E
2681.3382643	5080 \pm 15.3	-1116.0	-20.6	E
2888.6594807	5280 \pm 15.2	-916.0	5.3	E
3008.7783200	-387.63 \pm 3.93	-769.7	34.3	L
3251.0195300	-193.93 \pm 3.89	-576.0	-8.4	L
3280.9150400	-170.27 \pm 3.91	-552.4	-12.6	L
3311.5240765	5650 \pm 15.3	-546.0	-34.2	E
3337.6767600	-104.14 \pm 3.88	-486.3	1.9	L
3358.3409466	5720 \pm 15.5	-476.0	-6.2	E
3391.6575900	-58.13 \pm 3.32	-440.2	0.3	L
3954.9796600	357.90 \pm 4.19	-24.2	15.2	L
3957.9836700	363.23 \pm 3.42	-18.9	18.8	L
4071.8361900	366.27 \pm 6.76	-15.8	-39.8	L
4072.7411200	386.03 \pm 3.61	3.9	-20.5	L
4099.7956300	435.51 \pm 3.71	53.4	15.2	L
4135.6839700	441.76 \pm 3.98	59.6	3.5	L
4373.9683300	546.37 \pm 4.43	164.3	1.6	L
4723.9418500	690.14 \pm 4.06	308.0	21.5	L
4785.8204800	684.08 \pm 3.82	302.0	-3.0	L
5843.9587200	853.85 \pm 6.00	471.7	-33.4	L
6562.4748310	6874.0 \pm 4.3	552.9	9.4	S
6562.4821578	6876.4 \pm 4.3	555.3	11.8	S
6563.5081427	6896.2 \pm 4.1	575.1	31.6	S
6563.5154927	6895.6 \pm 4.1	574.5	31.0	S
6565.5432908	6855.2 \pm 4.2	534.1	-9.4	S
6565.5506060	6853.4 \pm 4.1	532.3	-11.2	S
6608.4598096	6871.2 \pm 4.2	550.1	6.6	S
6608.4677262	6871.9 \pm 4.1	550.8	7.3	S
6883.5463382	6846.3 \pm 4.2	525.2	-11.7	S
6883.5563276	6849.6 \pm 4.2	528.5	-8.4	S
6912.6107890	6863.1 \pm 4.3	542.0	6.4	S
6912.6198869	6870.0 \pm 4.3	548.9	13.3	S
6913.4711873	6860.5 \pm 4.3	539.4	3.9	S
6913.4797411	6860.4 \pm 4.3	539.3	3.8	S
6946.4649120	6836.4 \pm 4.1	515.3	-18.5	S
6946.4722502	6837.0 \pm 4.1	515.9	-17.9	S
7062.2501790	6839.4 \pm 4.3	518.3	-8.0	S
7062.2613470	6840.3 \pm 4.5	519.2	-7.1	S
7062.2731630	6847.0 \pm 4.4	525.9	-0.4	S
7236.6208314	6818.8 \pm 4.1	497.7	-12.9	S

TABLE 7 — *Continued*

BJD -2450000	RV \pm err (m s^{-1})	RV- γ (m s^{-1})	O-C (m s^{-1})	Sp. ^a
7236.6298368	6819.2 \pm 4.1	498.1	-12.5	S
7296.4982802	6828.1 \pm 4.1	507.0	3.1	S
7296.5072853	6827.9 \pm 4.1	506.8	2.9	S
7448.2976778	6801.0 \pm 4.3	479.9	-3.7	S
7448.3083946	6799.6 \pm 4.4	478.5	-5.1	S

^a “E” stands for ELODIE, “H” for Hamilton, and “S” for SOPHIE spectrograph.

REFERENCES

- Anderson, J. 2006, in *The 2005 HST Calibration Workshop: Hubble After the Transition to Two-Gyro Mode*, ed. A. M. Koekemoer, P. Goudfrooij, & L. L. Dressel, 11
- Anderson, J., & King, I. R. 2004, *Multi-filter PSFs and Distortion Corrections for the HRC*, Tech. rep.
- Baraffe, I., Homeier, D., Allard, F., & Chabrier, G. 2015, *A&A*, 577, A42
- Baranne, A., Queloz, D., Mayor, M., et al. 1996, *A&AS*, 119, 373
- Barnes, S. A. 2003, *ApJ*, 586, 464
- . 2007, *ApJ*, 669, 1167
- Beuzit, J.-L., Feldt, M., Dohlen, K., et al. 2008, in *Proc. SPIE*, Vol. 7014, 18
- Blanco-Cuaresma, S., Soubiran, C., Heiter, U., & Jofré, P. 2014, *A&A*, 569, A111
- Bouchy, F., Hébrard, G., Udry, S., et al. 2009, *A&A*, 505, 853
- Brandt, T. D., McElwain, M. W., Turner, E. L., et al. 2013, *ApJ*, 764, 183
- Brandt, T. D., Kuzuhara, M., McElwain, M. W., et al. 2014, *ApJ*, 786, 1
- Bressan, A., Marigo, P., Girardi, L., et al. 2012, *MNRAS*, 427, 127
- Caballero, J. A. 2010, *A&A*, 514, A98
- Chabrier, G. 2003, *PASP*, 115, 763
- Chauvin, G., Lagrange, A.-M., Dumas, C., et al. 2004, *A&A*, 425, L29
- Chen, Y., Girardi, L., Bressan, A., et al. 2014, *MNRAS*, 444, 2525
- Crepp, J. R., Johnson, J. A., Howard, A. W., et al. 2014, *ApJ*, 781, 29
- . 2013a, *ApJ*, 774, 1
- Crepp, J. R., Johnson, J. A., Fischer, D. A., et al. 2012a, *ApJ*, 751, 97
- Crepp, J. R., Johnson, J. A., Howard, A. W., et al. 2012b, *ApJ*, 761, 39
- . 2013b, *ApJ*, 771, 46
- Currie, T., Daemgen, S., Debes, J., et al. 2014, *ApJ*, 780, L30
- Cutri, R. M., Skrutskie, M. F., van Dyk, S., et al. 2003, *VizieR Online Data Catalog*, 2246, 0
- Duquennoy, A., & Mayor, M. 1991, *A&A*, 248, 485
- Egner, S., Ikeda, Y., Watanabe, M., et al. 2010, in *Proc. SPIE*, Vol. 7736, 4
- Evans, T. M., Ireland, M. J., Kraus, A. L., et al. 2012, *ApJ*, 744, 120
- Fischer, D. A., Marcy, G. W., & Spronck, J. F. P. 2014, *ApJS*, 210, 5
- Flower, P. J. 1996, *ApJ*, 469, 355
- Ford, E. B. 2006, *ApJ*, 642, 505
- Granzner, T., Schüssler, M., Caligari, P., & Strassmeier, K. G. 2000, *A&A*, 355, 1087
- Gray, R. O., Corbally, C. J., Garrison, R. F., McFadden, M. T., & Robinson, P. E. 2003, *AJ*, 126, 2048
- Grether, D., & Lineweaver, C. H. 2006, *ApJ*, 640, 1051
- Grevesse, N., Asplund, M., & Sauval, A. J. 2007, *Space Sci. Rev.*, 130, 105
- Gustafsson, B., Edvardsson, B., Eriksson, K., et al. 2008, *A&A*, 486, 951
- Hashimoto, J., Dong, R., Kudo, T., et al. 2012, *ApJ*, 758, L19
- Hayano, Y., Takami, H., Oya, S., et al. 2010, in *Proc. SPIE*, Vol. 7736, 0
- Helminiak, K. G. 2009, *New Astronomy*, 14, 521
- Høg, E., Fabricius, C., Makarov, V. V., et al. 2000, *A&A*, 355, L27
- Holmberg, J., Nordström, B., & Andersen, J. 2009, *A&A*, 501, 941
- Isaacson, H., & Fischer, D. 2010, *ApJ*, 725, 875
- Janson, M., Brandt, T. D., Kuzuhara, M., et al. 2013, *ApJ*, 778, L4
- Jovanovic, N., Martinache, F., Guyon, O., et al. 2015, *PASP*, 127, 890
- Kovtyukh, V. V., Soubiran, C., & Belik, S. I. 2004, *A&A*, 427, 933
- Kupka, F., Dubernet, M.-L., & VAMDC Collaboration. 2011, *Baltic Astronomy*, 20, 503
- Kuzuhara, M., Tamura, M., Kudo, T., et al. 2013, *ApJ*, 774, 11
- Lagrange, A.-M., Gratadour, D., Chauvin, G., et al. 2009, *A&A*, 493, L21
- Latham, D. W., Stefanik, R. P., Mazeh, T., Mayor, M., & Burki, G. 1989, *Nature*, 339, 38
- Macintosh, B., Graham, J. R., Ingraham, P., et al. 2014, *Proceedings of the National Academy of Science*, 111, 12661
- Mamajek, E. E. 2012, *ApJ*, 754, L20
- Mamajek, E. E., & Hillenbrand, L. A. 2008, *ApJ*, 687, 1264
- Mamajek, E. E., Bartlett, J. L., Seifahrt, A., et al. 2013, *AJ*, 146, 154
- Marcy, G. W., & Butler, R. P. 2000, *PASP*, 112, 137
- Marois, C., Lafrenière, D., Doyon, R., Macintosh, B., & Nadeau, D. 2006, *ApJ*, 641, 556
- Marois, C., Macintosh, B., Barman, T., et al. 2008, *Science*, 322, 1348
- Martinache, F., Guyon, O., Jovanovic, N., et al. 2014, *PASP*, 126, 565
- Mathar, R. J. 2004, *Appl. Opt.*, 43, 928
- . 2007, *Journal of Optics A: Pure and Applied Optics*, 9, 470
- Mayor, M., & Queloz, D. 1995, *Nature*, 378, 355
- Metchev, S. A., & Hillenbrand, L. A. 2009, *ApJS*, 181, 62
- Monnier, J. D., Che, X., Zhao, M., et al. 2012, *ApJ*, 761, L3
- Montes, D., López-Santiago, J., Gálvez, M. C., et al. 2001, *MNRAS*, 328, 45
- Moutaka, J., Ilovaisky, S., Prugniel, P., & Soubiran, C. 2004, in *SF2A-2004: Semaine de l’Astrophysique Française*, ed. F. Combes, D. Barret, T. Contini, F. Meynadier, & L. Pagani, 547
- Myers, J. R., Sande, C. B., Miller, A. C., Warren, Jr., W. H., & Tracewell, D. A. 2015, *VizieR Online Data Catalog*, 5145, 0
- Narita, N., Kudo, T., Bergfors, C., et al. 2010, *PASJ*, 62, 779
- Narita, N., Takahashi, Y. H., Kuzuhara, M., et al. 2012, *PASJ*, 64, L7
- Noyes, R. W., Hartmann, L. W., Baliunas, S. L., Duncan, D. K., & Vaughan, A. H. 1984, *ApJ*, 279, 763
- Pace, G. 2013, *A&A*, 551, L8
- Perrier, C., Sivan, J.-P., Naef, D., et al. 2003, *A&A*, 410, 1039
- Perryman, M. A. C., Lindegren, L., Kovalevsky, J., et al. 1997, *A&A*, 323, L49
- Rameau, J., Chauvin, G., Lagrange, A.-M., et al. 2013, *ApJ*, 772, L15
- Riddle, R. L., Tokovinin, A., Mason, B. D., et al. 2015, *ApJ*, 799, 4
- Ryu, T., Sato, B., Kuzuhara, M., et al. 2016, *ApJ*, 825, 127
- Sanchis-Ojeda, R., Winn, J. N., Marcy, G. W., et al. 2013, *ApJ*, 775, 54
- Sato, B., Fischer, D. A., Ida, S., et al. 2009, *ApJ*, 703, 671
- Skumanich, A. 1972, *ApJ*, 171, 565
- Soubiran, C., Jasiewicz, G., Chemin, L., et al. 2013, *A&A*, 552, A64
- Strassmeier, K., Washuettl, A., Granzner, T., Scheck, M., & Weber, M. 2000, *A&AS*, 142, 275
- Strassmeier, K. G., & Rice, J. B. 1998, *A&A*, 330, 685
- Suzuki, R., Kudo, T., Hashimoto, J., et al. 2010, in *Proc. SPIE*, Vol. 7735, 30
- Takeda, Y., Kawanomoto, S., Honda, S., Ando, H., & Sakurai, T. 2007, *A&A*, 468, 663
- Tamura, M. 2009, in *AIP Conf. Ser.*, ed. T. Usuda, M. Tamura, & M. Ishii, Vol. 1158, 11–16
- Thalmann, C., Janson, M., Buenzli, E., et al. 2011, *ApJ*, 743, L6
- Tokovinin, A. 2014, *AJ*, 147, 86
- Torres, G. 2010, *AJ*, 140, 1158
- Valenti, J. A., & Fischer, D. A. 2005, *ApJS*, 159, 141
- van der Marel, R. P., Anderson, J., Cox, C., et al. 2007, *Calibration of ACS/WFC Absolute Scale and Rotation for Use in creation of a JWST Astrometric Reference Field*, Tech. rep.
- van Leeuwen, F. 2007, *A&A*, 474, 653
- Voges, W., Aschenbach, B., Boller, T., et al. 1999, *A&A*, 349, 389

- White, R. J., Gabor, J. M., & Hillenbrand, L. A. 2007, *AJ*, 133, 2524
- Wilson, P. A., Hébrard, G., Santos, N. C., et al. 2016, *A&A*, 588, A144
- Wright, J. T., Marcy, G. W., Butler, R. P., & Vogt, S. S. 2004, *ApJS*, 152, 261
- Yadav, R. K., Gastine, T., Christensen, U. R., & Reiners, A. 2015, *A&A*, 573, A68
- Zuckerman, B., Vican, L., Song, I., & Schneider, A. 2013, *ApJ*, 778, 5